RSC Advances

PAPER

View Article Online
View Journal | View Issue

Cite this: *RSC Adv.*, 2021, **11**, 9880

Synthesis of gallotannin capped iron oxide nanoparticles and their broad spectrum biological applications†

Bilal Ahmed, *[ac] Asad Syed, [b] Khursheed Ali,[c] Abdallah M. Elgorban,[b] Afroz Khan,[d] Jintae Lee*[a] and Hind A. AL-Shwaiman[b]

Green synthesized nanoparticles (NPs) have attracted enormous attention for their clinical and non-clinical applications. A natural polyphenol, gallo-tannin (GT) was used to reduce and cap the Fe_2O_3-NPs. GT-Fe_2O_3-NPs were synthesized following co-precipitation of $FeCl_3$ and $FeSO_4 \cdot 7H_2O$ with GT. Fe_2O_3-NPs absorbed light at 380 nm. Physicochemically, Fe_2O_3-NPs were spherical with slight aggregation and average diameter of 12.85 nm. X-ray diffraction confirmed crystallinity and EDX revealed the elemental percentage of iron and oxygen as 21.7% and 42.11%, respectively. FT-IR data confirmed the adsorption of gallo-tannin functional groups. Multiple drug-resistant (MDR) *Escherichia coli* (ESβL), *Pseudomonas aeruginosa* (ESβL), and *Staphylococcus aureus* were found susceptible to 500–1000 μg GT-Fe_2O_3-NPs per ml. In synergy, Fe_2O_3-NPs enhanced the efficiency of some antibiotics. GT-Fe_2O_3 NPs showed significant ($P \leq 0.05$) inhibition of growth and biofilm against MDR *E. coli*, *P. aeruginosa*, and *S. aureus* causing morphological and biofilm destruction. Violacein production (quorum sensing mediated) by *C. violaceum* was inhibited by GT-Fe_2O_3-NPs in a concentration-dependent manner with a maximum decrease of 3.1-fold. A decrease of 11-fold and 2.32-fold in fungal mycelial growth and human breast cancer (MCF-7) cell viability, respectively was evident. This study suggests a plausible role of gallo-tannin capped Fe_2O_3-NPs as an alternative antibacterial, antiquorum sensing, antibiofilm, antifungal, and anti-proliferative agent.

Received 11th January 2021
Accepted 23rd February 2021

DOI: 10.1039/d1ra00220a

rsc.li/rsc-advances

1 Introduction

Nanotechnology has the potential to manipulate materials at molecular and atomic scale giving them unique physicochemical features over their bulk materials.[1] Among nanomaterials, the magnetic ferric(III) oxide (Fe_2O_3) nanoparticle is a stable oxide of iron possessing anti-ferromagnetic and n-type semiconducting features that arise from its 2.1 eV bandgap.[2] It has a wide range of applications as gas sensors, magnetic materials, pigments, and catalysts, in lithium-ion batteries and enhanced magnetic resonance (MR) imaging.[3] However, the interaction of bare surface Fe_2O_3 nanoparticles and hence their toxicity to biological systems and environment reduce their application in the biomedical field.[4] To overcome this, Fe_2O_3 nanoparticles can be surface functionalized by green biomolecules reducing their toxicity to the environment while providing the target specificity. In this line, some water-soluble polymers have been used such as starch, dextran, polysaccharides, chitosan, protein, and gum Arabic that enhanced the bioactivity of Fe_2O_3 nanoparticles.[5–8] Moreover, the conjugation of phyto-constituents with nanoparticles at nucleation stage remarkably improves their stabilization and dispersity in an aqueous solution.[9]

Like some other metal oxide nanoparticles, Fe_2O_3 nanoparticles have shown polymorphism in their crystalline structure such as rhomboidal (α-Fe_2O_3), cubic centered (β-Fe_2O_3), cubic (γ-Fe_2O_3), and orthorhombic (ε-Fe_2O_3).[10,11] Though, iron oxides species are more readily oxidized in solutions as compared to other metal nanoparticles such as gold (Au) and silver (Ag). For various applications, Fe_2O_3 and Fe_3O_4 nanoparticles have been fabricated using extracts of *Camellia sinensis*,[12] *Aloe vera*,[13] *Cymbopogon citratus*,[14] and *Pheonix dactylifera*.[15] Toxicity could be overwhelmed by NP's capping through a benign green polymer like gallo-tannin. Attempts have been made to prepare bioactive Fe_2O_3 nanoparticles by capping of polymers such as polyvinylpyrrolidone (PVP)[16] and antioxidants like quercetin.[17] Few studies report tannic acid mediated synthesis of iron oxide nanoparticles (IONPs) but with other

[a]*School of Chemical Engineering, Yeungnam University, Gyeongsan, Republic of Korea. E-mail: jtlee@ynu.ac.kr*

[b]*Department of Botany and Microbiology, College of Science, King Saud University, P.O. Box 2455, Riyadh 11451, Saudi Arabia*

[c]*Department of Agricultural Microbiology, Faculty of Agricultural Sciences, Aligarh Muslim University, Aligarh 202002, India. E-mail: bilalahmed.amu@gmail.com*

[d]*Department of Physics, Faculty of Science, Aligarh Muslim University, Aligarh 202002, India*

† Electronic supplementary information (ESI) available. See DOI: 10.1039/d1ra00220a

methods and experimental conditions, for example, by dissolving iron in distilled water in the presence of tannic acid but without any evidence of its biological activity.[18] None of the previous studies on tannic acid mediated synthesis of IONPs have shown or focused on broad-spectrum antibacterial and antibiofilm activity along with antiquorum sensing, antifungal, and anti-proliferative potential which are extremely important for their clinical use.

Multiple drug resistance (MDR) in clinical pathogenic bacteria is globally a growing menace due to overuse or underuse of antibiotics resulting in one or the other MDR.[19] As per the reports of the World Health Organization (WHO), MDR in causal agents of infected chronic wounds, gonorrhea, pneumonia, and tuberculosis is of higher medical concern due to the fatality of unsuccessful medical implants and other complications in addition to economic losses.[20,21] Development of resistance starts from the sensing of an adequate bacterial quorum governed by the special molecules called *N*-acyl-homoserine lactones (AHLs) resulting in bacterial virulence and biofilm formation. With the advent of nanotechnology, biologically capped nanoparticles could be a choice of treatment due to their unique physicochemical features over their micro or bulk-sized particles.[22,23] However, the morphology, chemical composition, surface capping, and method of synthesis of nanoparticles impact the antibacterial and antibiofilm activities.[24] The antibacterial and antibiofilm potential of Fe_2O_3 nanoparticles have also been reported in few studies on drug resistant bacteria such as *S. aureus*,[25–28] *E. coli*,[26–28] *Micrococcus luteus*,[26] *Klebsiella pneumoniae*,[26,27] *P. aeruginosa*,[26] *Bacillus subtilis*,[26,27] *Serratia marcescens*,[26] and *S. epidermidis*.[26]

Similarly, breast cancer among all other cancers is a major clinical challenge and the fourth frequently diagnosed cancer in the USA. For example, human epithelial breast cancer cells (MCF-7) have developed MDR against many drugs including paclitaxel and doxorubicin.[29] The behavior of cancer cells is very dynamic and complex which needs both target specific and stable anticancer therapeutics. This demand can be fulfilled by synthesizing novel biologically capped nanoparticles with enhanced pharmacokinetics. MCF-7 cell line has been used in earlier studies as a model due to their high affinity towards iron oxide nanoparticles and their higher uptake.[30,31] Fe_2O_3-NPs exert cytotoxicity by inducing apoptosis, reactive oxygen species, dissipation of mitochondrial membrane potential, and lipid oxidative damage.[30,32] Furthermore, the low efficiency of many agrochemicals to pathogenic fungus like *F. oxysporum* has increased the demand for new nano-based materials. Iron oxide nanoparticles synthesized through plant extracts have shown low to high antifungal performance. Some examples include growth inhibition of *Aspergillus flavus* by Fe_2O_3 nanoparticles synthesized using reducing extract of *Hyphaene thebaica*[33] and broad-spectrum antifungal activity of *Papaver somniferum* mediated Fe_2O_3 nanoparticles to *A. fumigatus*, *A. flavus*, *A. niger*, and *Fusarium solani*.[34]

To combat these pathogens and drug resistance in bacterial, fungal and cancerous cells, the gallo-tannin capped Fe_2O_3 nanoparticles could be a promising alternative which have not been tested for broad-spectrum biological use. Therefore, this study was systematically designed to achieve the (i) green Fe_2O_3 nanoparticles capped by gallo-tannin, (ii) their physicochemical characterization determining structure, morphology, size, elemental composition, and adsorbed functional groups (iii) antibacterial and antibiofilm activities against drug-resistant Gram-negative and Gram-positive bacteria, (iv) anti-quorum sensing activity using *C. violaceum*, (v) antifungal activity against *F. oxysporum*, and (vi) anticancer activity against MCF-7 cell line.

2 Materials and methods

2.1 Chemicals and reagents

Gallo-tannin ($C_{76}H_{52}O_{46}$) (product code-GRM7541; Hi-LR grade), NaOH flakes (product code-GRM604), Luria Bertani (LB) agar (product code-M1151), antibiotic discs, glutaraldehyde solution 25% w/w (product code-RM5927), 4% paraformaldehyde solution (product code-TCL119), crystal violet (product code-GRM961; practical grade), rose bengal agar base (product code-M842), Dulbecco's modified eagle's medium (product code-AT186), and 3-(4,5-dimethylthiazol-2-yl)-2,5-diphenyl tetrazolium bromide (MTT; product code-TC191) were procured from HiMedia, Mumbai, India. Iron(III) chloride (product code-72287, 98% purity) and iron(II) sulfate heptahydrate (product code-97868, 99.5% purity) were purchased from Sisco Research Laboratories (SRL), Mumbai, India. The phosphate-buffered saline (PBS 1X) was prepared in sterile distilled water (NaCl 8 g l^{-1}, KCl 0.2 g l^{-1}, Na_2HPO_4 1.44 g l^{-1}, and KH_2PO_4 0.24 g l^{-1}). Dimethyl sulfoxide (product code-102952, ACS grade) was obtained from Merck Life Science Private Limited, Mumbai, India.

2.2 Microbial cultures and cell line

Clinical cultures of *E. coli, P. aeruginosa*, and *S. aureus* were obtained from culture stock of Jawaharlal Nehru Medical College (a tertiary care hospital), Aligarh Muslim University, Aligarh, India that were originally isolated from pus/wound samples of the registered patients. Standard strains of *E. coli* (ATCC 25922), *P. aeruginosa* (ATCC 27853), and *S. aureus* (ATCC 9144) were also used as control. *C. violaceum* obtained from ATCC (12472) was used for antiquorum sensing experiments. Bacterial cultures were regularly revived and maintained in the laboratory. Cultures were maintained in three sets: (i) on agar plates at 4 °C, (ii) as glycerol cultures kept at −80 °C, and (iii) lyophilized powder. *F. oxysporum* was obtained from ATCC (62506). The MCF-7 (Michigan Cancer Foundation-7) cells (ATCC; Manassas, USA) were used for assessing the anticancer potential of GT-Fe_2O_3 nanoparticles.

2.3 Synthesis and characterization of GT-Fe_2O_3 nanoparticles

The GT-Fe_2O_3 nanoparticles were synthesized following a co-precipitation method (Fig. 1). Briefly, a 100 ml hot iron solution containing $FeCl_3$ (0.1 M) and $FeSO_4$ (0.05 M) as precursors were mixed with 50 ml hot gallo-tannin ($C_{76}H_{52}O_{46}$) solution (30 mM). The heating was lowered up to ~40 °C and maintained for

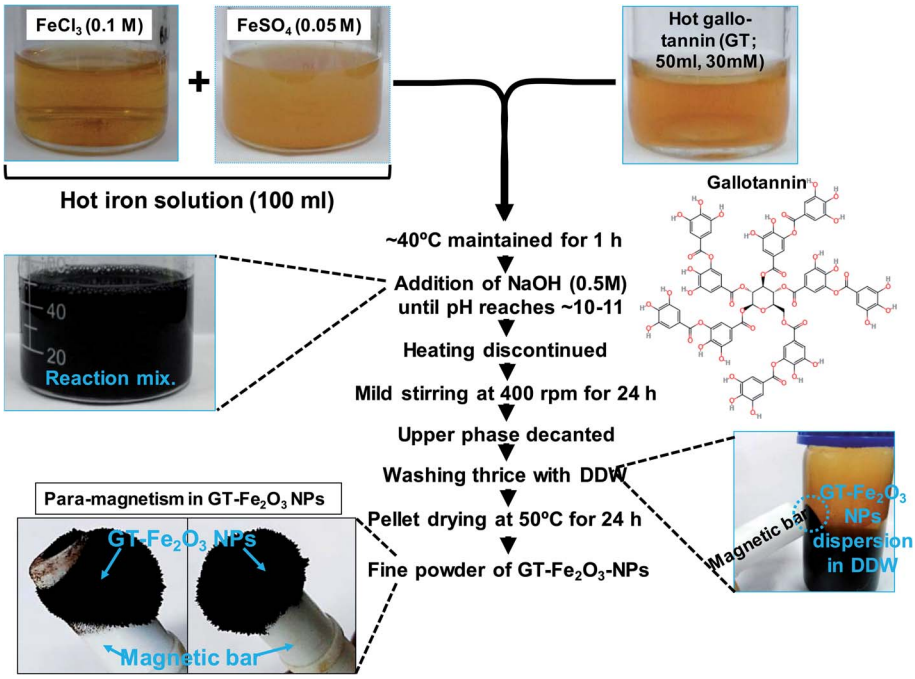

Fig. 1 A stepwise method developed for the synthesis of gallo-tannin capped magnetic Fe_2O_3 nanoparticles (NPs).

1 h. The pH of the solution was maintained up to 11.0 using 0.5 M NaOH solution. The pellet was rinsed with double distilled water at least five times followed by drying at 50 °C for 24 h. The fine powder of GT-Fe_2O_3 nanoparticles was obtained and characterized by UV-Vis, EDX, SEM, AFM, TEM, and FT-IR following our previous methods.[35] The GT-Fe_2O_3 nanoparticles were evaluated for antibacterial, antibiofilm, anti-quorum sensing, antifungal, and anticancer activities.

2.4 *In vitro* antimicrobial susceptibility determination

A 0.1 ml culture equivalent to a 0.5 McFarland standard from each of the three test bacterial strains was spread plated on Luria Bertani (LB) agar. To check the susceptibility or resistance to antimicrobial drugs, discs of amikacin (30 μg per disc), amoxicillin (10 μg per disc), azithromycin (15 μg per disc), cefoperazone (75 μg per disc), chloramphenicol (30 μg per disc), gatifloxacin (5 μg per disc), gentamycin (10 μg per disc), levofloxacin (5 μg per disc), lomefloxacin (10 μg per disc), nalidixic acid (30 μg per disc), norfloxacin (10 μg per disc), ofloxacin (5 μg per disc), penicillin G (2 units), and tetracycline (10 μg per disc) were used. Drug susceptibility testing was performed by Kirby–Bauer disc diffusion method following the recommendations of the Clinical and Laboratory Standards Institute (CLSI, 2016).[36,37] Discs of antibiotics were placed on LB agar plates containing bacterial cultures and allowed to incubate for 18 h at 37 °C for the bacterial lawn to appear. A clear zone around (halo) antibiotic discs was measured and explained as per the criteria of CLSI.[37] Type strains of *P. aeruginosa* (ATCC 27853), *E. coli* (ATCC 25922), and *S. aureus* (ATCC 9144) were also used as reference and the sensitivity/resistance was described following our earlier method.[38]

2.5 Confirmatory test for extended spectrum β-lactamase (ESβL) *E. coli* and *P. aeruginosa*

To screen the ESβL producing *E. coli* and *P. aeruginosa*, a method similar to *in vitro* antimicrobial testing was followed using 30 μg potency discs of each cefotaxime, ceftazidime, ceftriaxone, and cefepime. The zone of inhibition around discs was measured and interpreted as per CLSI, 2016 guidelines.[38] Reduced sensitivity shown by bacterial cultures to these drugs indicated that bacterial cultures were potent ESβL producers. For confirmation, bacteria were subjected to double-disc synergy testing. Two antibiotics, ceftazidime, and cefotaxime (30 μg per disc of each) were tested alone and in combination with clavulanic acid (10 μg per disc). The single and dual discs of (i) cefotaxime/ceftazidime (30 μg per disc) alone and (ii) cefotaxime/ceftazidime (30 μg per disc) + clavulanic acid (10 μg per disc) were placed on LB agar plates (spread with bacterial cultures) at a distance of at least 20 mm. After incubation for 24 h at 37 °C, the zone of inhibition was recorded and checked for ≥5 mm increase in zone diameter by cefotaxime/ceftazidime (30 μg per disc) + clavulanic acid (10 μg per disc) as compared to cefotaxime/ceftazidime (30 μg per disc) alone.

2.6 Antibacterial activity of GT-Fe_2O_3 nanoparticles

Agar well diffusion assay was performed for the screening of antibacterial potential along with positive (imipenem, 10 μg per disc) and negative (PBS 1X) controls.[39] The synergistic effect of GT-Fe_2O_3 nanoparticles with the following antibiotics was also assessed: amikacin (30 μg per disc), amoxicillin (10 μg per disc), azithromycin (15 μg per disc), cefoperazone (75 μg per disc), chloramphenicol (30 μg per disc), gatifloxacin (5 μg per disc), gentamycin (10 μg per disc), levofloxacin (5 μg per disc),

lomefloxacin (10 μg per disc), nalidixic acid (30 μg per disc), norfloxacin (10 μg per disc), ofloxacin (5 μg per disc), penicillin G (2 units), and tetracycline (10 μg per disc). The minimum inhibitory concentration (MIC) was determined by growing the bacterial cultures with 15.62–1000 μg ml^{-1} GT-Fe_2O_3 nanoparticles as described earlier.[35] Dose–response curves were also plotted as $\log_{10}$ CFU ml^{-1} *vs.* nanoparticle concentration.

2.7 Morphological destruction of bacterial cells by GT-Fe_2O_3 nanoparticles

To determine the cellular destruction caused by GT-Fe_2O_3 nanoparticles, SEM analysis of untreated Gram-negative (*P. aeruginosa*) and Gram-positive (*S. aureus*) and cells treated with 500 μg ml^{-1} GT-Fe_2O_3 nanoparticles was performed. Briefly, overnight grown bacterial cultures (50 ml) were pelleted at 5000×*g*, washed thrice with PBS (1X), and the pellets were re-suspended in 10 ml PBS (1X). Cell suspension for each bacterial culture was divided into two. Five ml suspension was used as untreated control whereas, the other 5 ml was mixed with 500 μg ml^{-1} GT-Fe_2O_3 nanoparticles and allowed to incubate at 37 °C for 4 h in an incubator shaker (120 rpm). Afterward, cell suspensions were centrifuged (5000×*g*), washed thrice with PBS (1X), and fixed in 2.5% solution of glutaraldehyde and 2% paraformaldehyde initially at room temperature for 30 min. and then at 4 °C for 6 h with intermittent manual shaking. Fixative was removed from the samples by washing with PBS (1X). Samples were dehydrated with an ethanol gradient of 10%, 30%, 50%, 70%, 90%, and 100%, 10 min in each. Dehydrated samples were observed by field emission scanning electron microscopy (FE-SEM; QUANTA 200 FEG, FEI The Netherlands) following our earlier method.[40]

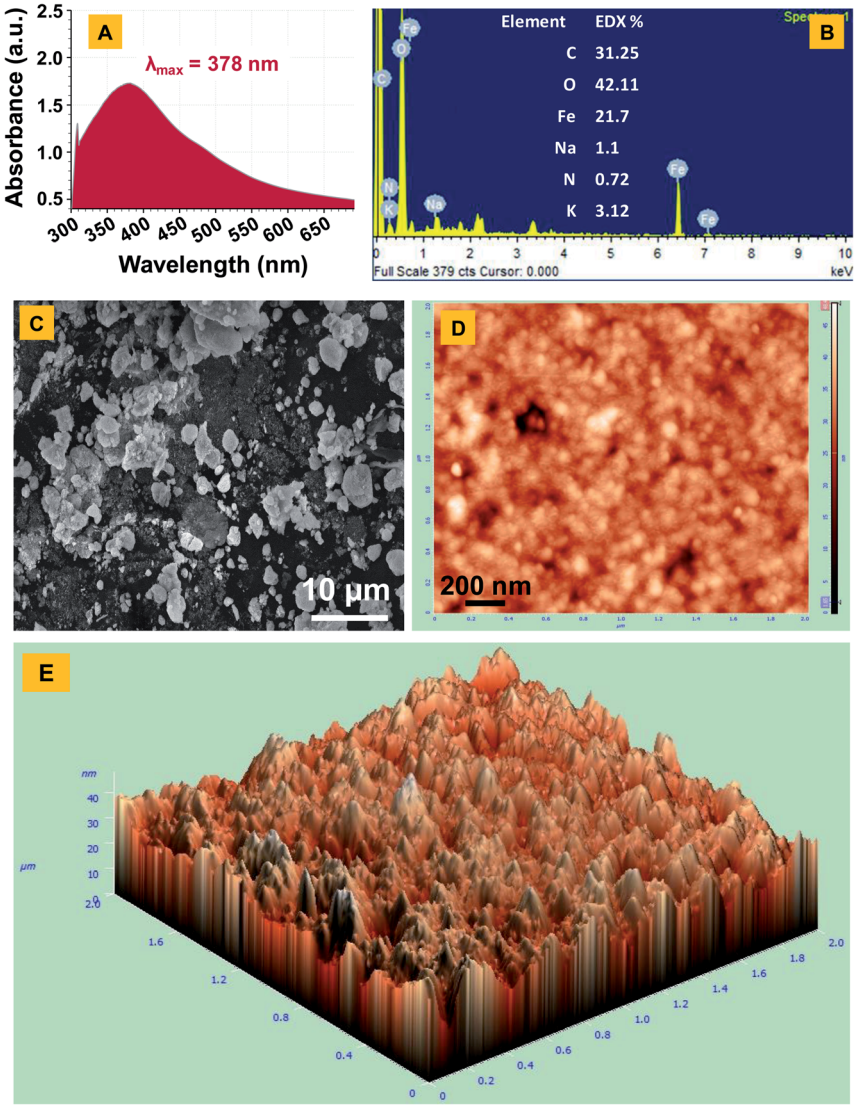

Fig. 2 UV-visible spectrum (panel A), EDX spectrum (panel B), SEM micrograph (panel C), 2D-AFM micrograph (panel D), and 3D-AFM micrograph (panel E) of Fe_2O_3 nanoparticles. λ_{max} in panel A stands for the wavelength (378 nm) at which GT-Fe_2O_3 nanoparticles has the strongest photon absorption. Symbols C, O, Fe, Na, N, and K in panel B represent carbon, oxygen, iron, sodium, nitrogen, and potassium, respectively.

2.8 Anti-quorum sensing (anti-QS) and antibiofilm activity

GT-Fe_2O_3 nanoparticles at 62.5, 125, 250, and 500 μg ml^{-1} were tested for anti-QS activity using the agar plate well diffusion method. A 0.1 ml culture of acyl-homoserine-lactone (AHL) overproducing *C. violaceum* (ATCC-12472) was mixed with 5 ml molten LB agar (0.4% w/v) and uniformly spread over LB agar in Petri plate. After solidification, wells of 6 mm diameter were prepared and the base was sealed with 0.7% sterile agar followed by the addition of 62.5–500 μg ml^{-1} GT-Fe_2O_3 nanoparticles to wells. After overnight incubation at 28 °C, the zone of violacein inhibition was measured. For quantification of violacein production under GT-Fe_2O_3 nanoparticle stress, *C. violaceum* culture (1.5 ml) overnight cultivated in GT-Fe_2O_3 nanoparticles amended LB broth was centrifuged (5000×*g*, 5 min) and the pellet was dissolved in DMSO (1 ml). After centrifugation of the DMSO mixture, the absorbance of the supernatant was measured at $\lambda_{max} = 585$ nm. Percent inhibition in violacein production over untreated control was calculated using the following formula: $[(control_{Abs=585nm} - treated_{Abs=585nm})/control_{Abs=585nm}] \times 100$. Antibiofilm activity of GT-Fe_2O_3 nanoparticles at MIC and two sub MICs ($\frac{1}{2}$ MIC and $\frac{1}{4}$ MIC) was evaluated employing crystal violet (0.1%) micro-dilution and cover slip methods with control.[41]

2.9 Antifungal activity of GT-Fe_2O_3 nanoparticles

The antifungal activity of GT-Fe_2O_3 nanoparticles against fungal pathogen *F. oxysporum* was assessed. Rose bengal agar media was amended with 125, 250, 500, and 1000 μg ml^{-1} GT-Fe_2O_3 nanoparticles and poured in Petri dishes. A ten days grown culture of *F. oxysporum* was smeared on an area of 1.5 cm in diameter on each Petri dish (control and treated) followed by incubation at 28 °C for six days with three replicates for each treatment and control. The mycelial growth (total area covered by fungus on a Petri dish) was measured and the percentage was calculated using the following formula:

Percent inhibition in mycelial growth = [(mycelial growth of control − mycelial growth of treatment)/mycelial growth of control] × 100.

The % fungal growth was plotted as a function of GT-Fe_2O_3 nanoparticles' concentration.

2.10 Anti-proliferative activity of GT-Fe_2O_3 nanoparticles

The human breast cancer cell line (MCF-7) was cultured as described in supplementary methods. Dulbecco's Modified Eagle's Medium (DMEM) was mixed with 31.25, 62.5, 125, and 250 μg ml^{-1} GT-Fe_2O_3 nanoparticles and sonicated (15 min at 40 W). MCF-7 cells (1×10^4 ml^{-1}) were then treated with nanoparticles for 24 h in DMEM medium. A microdilution method using 96-well plate was employed for 3-(4,5-dimethylthiazol-2-yl)-2,5-diphenyl tetrazolium bromide (MTT) assay. Following incubation, culture media was removed and cells were gently rinsed at least thrice with sterile PBS (1X). MTT was added at a rate of 5 mg ml^{-1} to each microtiter well followed by incubation at 37 °C for 4 h. Then, 0.2 ml DMSO was added to each well, and absorbance was recorded at $\lambda_{max} = 550$ nm. The data was presented as percent cell viability as a function of nanoparticle concentration.

2.11 Statistical analysis

Experiments were performed in triplicates and mean values were plotted as a function of nanoparticle concentration. Error

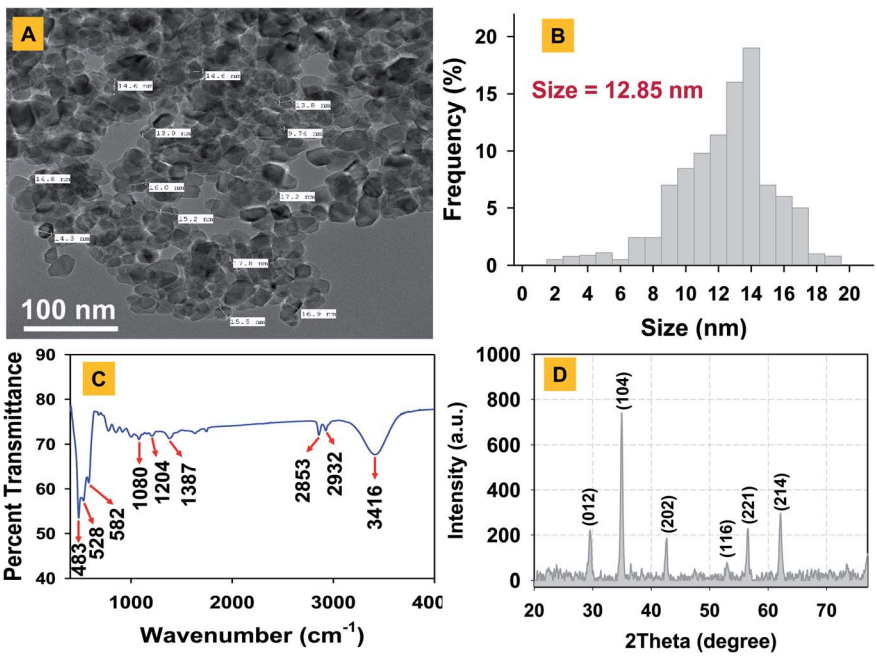

Fig. 3 TEM micrograph (panel A), frequency size distribution (panel B), FT-IR spectrum (panel C), and XRD pattern of GT-Fe_2O_3-nanoparticles (panel D). Down facing red arrows in panel C denotes different FT-IR signals in cm^{-1}.

bars represent the standard deviation (S.D.). Statistical significance among the treatments was calculated based on a 95% confidence limit ($P \leq 0.05$) using Student's *t*-test. Sigma plot 14.0 (Sigma plot, USA) was used to prepare graphs and statistical analyses.

3 Results and discussion

3.1 Synthesis and characterization of GT-Fe_2O_3 nanoparticles

The Fe_2O_3 nanoparticles were bio-fabricated using a green synthesis method employing gallo-tannin as a reducing and capping agent in alkaline conditions. This method has multiple advantages over physical and chemical methods such as its cost-effectiveness, rapid formation of Fe_2O_3 nanoparticles, environmentally non-toxic, and effective capping with a fairly small size of nanoparticles. The GT-Fe_2O_3 nanoparticles were synthesized by co-precipitation using gallo-tannin which is a polymer of gallic acid and glucose. Color of the reaction mixture changed instantly after mixing the hot iron solution and gallo-tannin, evident for GT-Fe_2O_3 nanoparticle synthesis (Fig. 1). Colloidal suspension and dried powder showed magnetism towards a magnetic bar. The GT-Fe_2O_3 nanoparticles, when scanned under UV-Vis range, revealed a maximum absorption at 380 nm (Fig. 2A). The black coloration of the solution could be explained due to the collective oscillation of electrons in the conduction band of zero-valent iron (Fe^0) which is known as surface plasmon resonance (SPR).[42] The EDX spectroscopic analysis of GT-Fe_2O_3 nanoparticles showed the percentage of iron (Fe) and oxygen (O) as 21.7% and 42.11%, respectively (Fig. 2B). Morphological analysis through SEM and AFM showed that nanoparticles formed

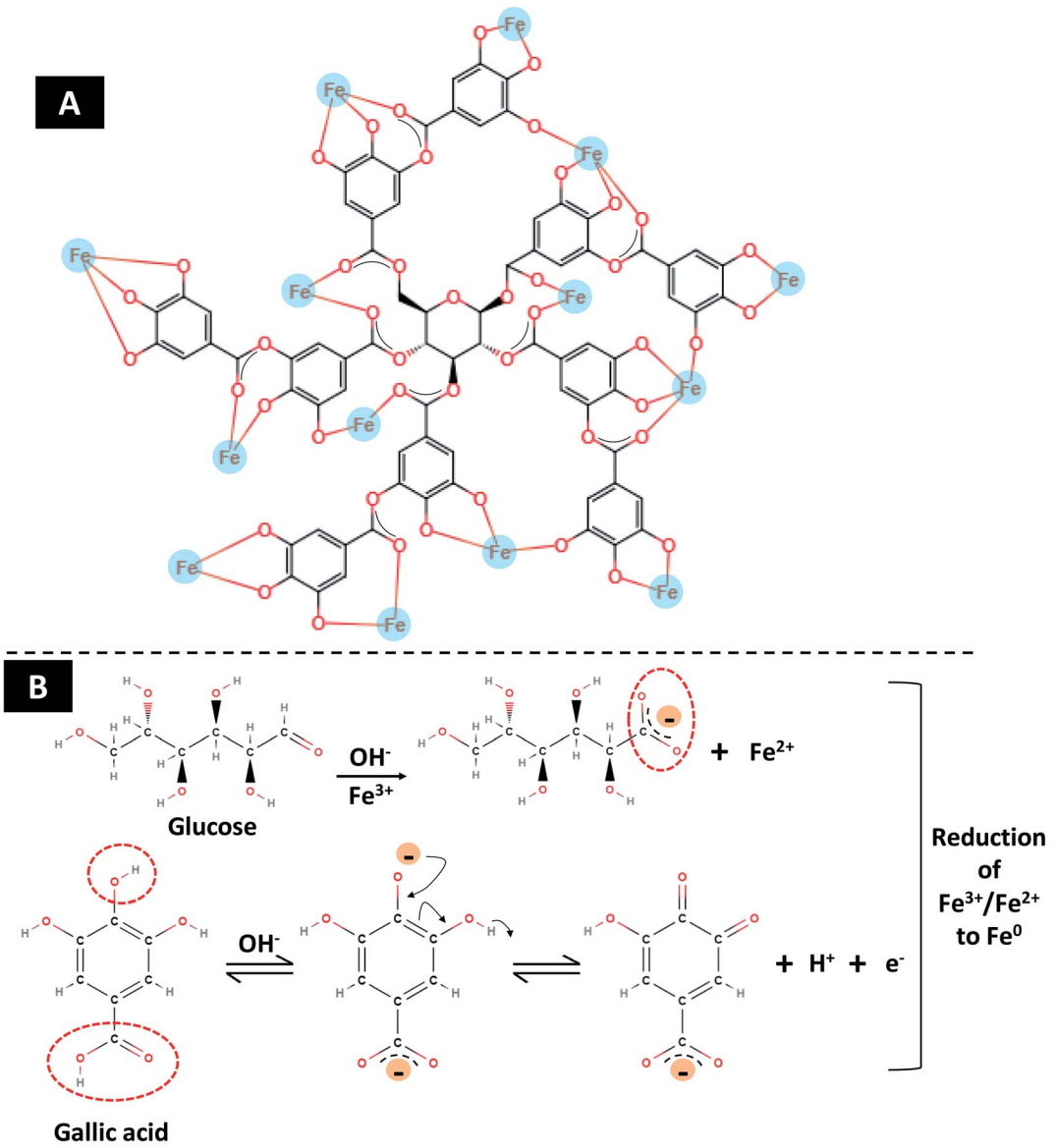

Fig. 4 Proposed stabilization of Fe ions by gallo-tannin (panel A) and possible reduction of Fe^{3+}/Fe^{2+} to Fe^0 by hydrolysable gallo-tannin (panel B). Quinine is formed as result of oxidation of –OH groups of tannin which release electrons for the reduction of iron salt.

were pleomorphic in shape with slight aggregation (Fig. 2C–E). This slight aggregation of GT-Fe_2O_3 nanoparticles is a result of polymer adherence and magnetic interaction between GT-Fe_2O_3 nanoparticles.[43] The shape observed under TEM was predominantly spherical (Fig. 3A) with an average particle size of 12.85 nm (Fig. 3B). The FT-IR spectral analysis also confirmed the formation of iron oxide nanoparticles with signals at 483 cm^{-1} for metal–oxygen vibration at the octahedral site (O ↔ Fe ↔ O), and 528 cm^{-1} and 582 cm^{-1} for metal–oxygen vibration at the tetrahedral site (Fe ↔ O) (Fig. 3C). The data also revealed the adsorption of –OH groups (signal at 3416 cm^{-1}) from gallic acid units. Peaks at 2932/2853 cm^{-1}, 1204 cm^{-1}, and 1080 cm^{-1} could be attributed to C–H stretching bands, C–O asymmetric stretching, and C–O–C or O–H absorption. These signals strongly advocate the involvement of polyphenolic groups of the polymer in the reduction of Fe^{3+}/Fe^{2+} and their interaction with reduced iron (Fe^0) atoms *via* C=O group.[44,45] Fig. 3D shows the XRD pattern of Fe_2O_3-NPs. The signals detected in XRD pattern can be well matched to alpha (α) phase Fe_2O_3-NPs with a close-packed oxygen lattice in rhombohedral centered hexagonal structure.[46] Miller indices (*hkl*) at 012, 104, 202, 116, 221, and 214 2θ° positions match with JCPDS file number of 84-308 as reported earlier.[47] The smaller size of Fe_2O_3 nanoparticles by gallo-tannin capping could be assigned to the chelation of iron cations by –OH and $–COO^-$ groups (Fig. 4A) forming a dark ferric/ferrous gallo-tannin. The bioactive capping around nanoparticles core could also contribute to the smaller size and magnetism of GT-Fe_2O_3 nanoparticles as reported earlier for hydrolyzable tannins.[48] Under alkaline conditions, as pH 10–11 in our method, the gallo-tannin undergoes hydrolysis and produces glucose and gallic acid.[49] Gallic acid units donate electrons in anionic form and convert into quinine form. Donated electrons reduce the Fe^{3+} and Fe^{2+} to Fe^0. The other product of hydrolysis, glucose also acts as a reducing agent converting Fe^{3+} to Fe^{2+} which is then converted to Fe^0 by quinine form of gallic acid.[50] Due to the presence of polyphenol groups, the stability of GT-Fe_2O_3 nanoparticles is sustained. The reduction and stabilization during GT-Fe_2O_3 nanoparticles synthesis can be summarized in the following steps: (i) interaction of –OH groups with Fe^{3+} and Fe^{2+} reduce them to Fe^0, (ii) gallic acid transforms to its quinine form due to oxidation, (iii) the –C=O group of quinine form of gallic acid units binds with zero-valent iron (Fe^0) stabilizing the growth of Fe_2O_3 nanoparticles and decide the shape and size of nanoparticles. A chemical depiction of this process is presented in Fig. 4B. The gallo-tannin could reduce the agglomeration of GT-Fe_2O_3 nanoparticles due to: (i) steric hindrance caused by phenol groups of gallo-tannin, (ii) coordination of Fe_2O_3 nanoparticles surface with –OH groups forming a surface monolayer thereby reducing the dipolar coupling between nanoparticle aggregates, (iii) solubility of GT-Fe_2O_3 nanoparticles in polar solvents due to the H-bonding at hydrophilic functional groups. When the GT-Fe_2O_3 nanoparticles were tested for their biological activities at various concentrations in different experimental conditions specific for each type of microorganism or cancer cells, a significant inhibition of growth was observed. The impact increased with increasing

Table 1 Detection of ESβLs producing *E. coli* and *P. aeruginosa* isolates

Bacteria	Antibiotics					DDST with clavulanate[a]			
	Cefotaxime (30 μg per disc)	Ceftazidime (30 μg per disc)	Cefepime (30 μg per disc)	Ceftriaxone (30 μg per disc)	Status	Cefotaxime + clavulanic acid (30 + 10 μg per disc)	Ceftazidime + clavulanic acid (30 + 10 μg per disc)	Result
E. coli ATCC 25922	31	30	33	31		32	32	
E. coli 104	14	19	0	0	Potent ESβL producer	19	22	Confirmed ESβL producer
P. aeruginosa ATCC 27853	22	27	29	22		24	28	
P. aeruginosa 148	20	20	15	15	Potent ESβL producer	26	25	Confirmed ESβL producer

[a] DDST = Double Disk Synergy Test; results are interpreted according to CLSI, 2006.

dose rate, however, at the lowest test concentration, the growth inhibitory or killing impact was found slightly higher than untreated control. Similar kind of trend of the effectivity of higher exposure concentration of nanoparticles has also been observed with metal oxide nanoparticles.[30,41,51]

3.2 Antibacterial activity of GT-Fe_2O_3 nanoparticles

Among test strains, *E. coli*-104 and *P. aeruginosa*-148 were found as ESβL producers (Table 1). This result suggests that the strain 104 and 148 were positive for extended-spectrum beta-lactamases enzymes. These enzymes confer resistance towards β-lactam antibiotics including the class of penicillins, cephalosporins, and monobactam aztreonam.[52] Due to this, the successful management of community and hospital-acquired infections becomes more complicated. The results of antimicrobial activity of antibiotics alone and in synergy with GT-Fe_2O_3 nanoparticles against drug-resistant strains are displayed in Table 2. GT-Fe_2O_3 nanoparticles increased the antibiotic efficiency against test pathogenic bacteria. The antibacterial potential of GT-Fe_2O_3 nanoparticles in combination with antibiotics displayed a considerable variation among antibiotics. For example, amoxicillin, ofloxacin, and gatifloxacin with GT-Fe_2O_3 nanoparticles showed a remarkable increase in the zone of inhibition as compared to antibiotics alone. Dose-dependent (15.62–1000 μg ml^{-1} GT-Fe_2O_3 nanoparticles) antibacterial assay showed inhibition of bacterial growth as a progressive reduction in the number of colony-forming units (CFU ml^{-1}) (Fig. 5A). The inhibition of CFUs at 750 μg ml^{-1} was found maximum for each bacterium which decreased as the concentration of nanoparticles went down. However, $\log_{10}$ CFU ml^{-1} was slightly lower than the control group at the lowest exposure concentration. MICs for *E. coli*, *P. aeruginosa*, and MRSA were determined as 750 μg ml^{-1}, 750 μg ml^{-1}, and 500 μg ml^{-1}, respectively. Results showed that all test concentrations of nanoparticles delayed the growth of all bacterial strains. Similarly, in a study, iron oxide nanoparticles were found effective against human bacterial species of *Escherichia*, and *Staphylococcus*, and *Bacillus* showing prominent zone of growth inhibition around agar wells as observed in our study.[53] Results suggested that the killing of bacterial cells could be due to morphological destruction of both Gram-negative (Fig. 5C) and Gram-positive cells (Fig. 5E) by GT-Fe_2O_3 nanoparticles. Untreated cells of *P. aeruginosa* (Fig. 5A) and *S. aureus* (Fig. 5B) were found with an intact cell envelope and smooth surface. However, when cells were treated with GT-Fe_2O_3 nanoparticles, substantial destruction of cell morphology and envelope was observed along with cellular debris adhered to around cells. Red arrows in Fig. 5C and E indicate cellular damage caused by GT-Fe_2O_3 nanoparticles. The damage was found severe in Gram-negative *P. aeruginosa* than Gram-positive *S. aureus* cells. This difference in the disruptive magnitude of GT-Fe_2O_3 nanoparticle toxicity could be explained by the structural composition of the bacterial cell envelope. The Gram-positive *S. aureus* cells possess a higher amount of peptidoglycan (PG; present as multiple layers of 15–80 nm) in the cell wall which could inhibit the uptake of nanoparticles to some extent over Gram-negative *P. aeruginosa* (single PG layer of 10 nm).[54] Similar to our results with Fe_2O_3-NPs, other nano species of metal-oxides including ZnO, CuO, Ag_2O, TiO_2 damage the cellular morphology and metabolism of *E. coli*, *P. aeruginosa*, *E. faecalis*, *Bacillus* sp., *Klebsiella pneumoniae*, *etc.* isolated frequently from clinical samples.[55] In a study, five metal-oxide NPs Al_2O_3, Fe_3O_4, CeO_2, ZrO_2, and MgO were tested against urinary tract bacterial

Table 2 Antibiotics used to check the drug resistance or susceptibility of test clinical bacteria and synergistic effect of GT-Fe_2O_3 nanoparticles with various antibiotics[a]

			Zone of inhibition (mm)					
			Antibiotic alone			Antibiotic in synergy with GT-Fe_2O_3 nanoparticles (500 μg ml^{-1})		
Antibiotic	Abbreviation	Potency (μg) per disc	*E. coli* 104	*P. aeruginosa* 148	MR *S. aureus* 112	*E. coli* 104	*P. aeruginosa* 148	MR *S. aureus* 112
Nalidixic acid	NA	30	0^R	10^R	0^R	20	19	17
Chloramphenicol	C	30	22^S	10^R	14^I	28	18	29
Tetracycline	TE	10	0^R	12^R	15^I	19	20	28
Penicillin G	P	2 units	13^R	10^R	0^R	20	21	21
Norfloxacin	NX	10	13^I	13^I	16^I	17	19	23
Azithromycin	AZM	15	0^R	10^R	0^R	19	19	17
Lomefloxacin	LOM	10	16^R	10^R	13^R	17	21	15
Levofloxacin	LE	5	16^I	18^I	27^S	18	19	29
Cefoperazone	CFP	75	20^I	0^R	18^I	22	18	20
Amikacin	AK	30	13^R	10^R	14	19	10	21
Amoxycillin	AMX	10	0^R	0^R	0^R	15	16	18
Gentamycin	GEN	10	12^R	0^R	12^R	17	18	19
Ofloxacin	OF	5	0^R	0^R	0^R	20	15	17
Gatifloxacin	GAT	5	0^R	0^R	0^R	21	19	19

[a] R = resistant; I = intermediate; S = sensitive.

pathogens such as *S. aureus*, *E. coli*, *P. morganii*, *Klebsiella* sp., *Enterobacter* sp., and *Pseudomonas* sp.[56] Results showed that Fe_3O_4-NPs were effective against *Enterobacter* sp. and *E. coli* only. The accurate mechanism of antibacterial activity of GT-Fe_2O_3 nanoparticles is not entirely known, however, it can be postulated that GT-Fe_2O_3 nanoparticles electrostatically interacts with bacterial cell wall/membrane resulting in loss of metabolism and killing of bacterial cells.[57]

3.3 Anti-QS and antibiofilm activity of GT-Fe_2O_3 nanoparticles

The GT-Fe_2O_3 nanoparticles were evaluated for possible interference with the QS signaling pathway of the bacterium *C. violaceum* both qualitatively and quantitatively. The QS signaling system in bacteria is a cell-to-cell chemical communication system that allows the bacterial population to effectively express their virulence in response to a threshold number of other cells of the same species required to cause pathogenesis. Biofilm formation is among those major virulence factors of pathogenic bacteria.[58] In our study, we have used *C. violaceum* (Gram-negative, facultative anaerobe, and rod-shaped bacterium) that is an autoinducer (*N*-acylated homoserine lactones) overproducing bacterial strain and has also been tested in some other studied as a QS indicator organism.[59,60] The GT-Fe_2O_3 nanoparticles at four test concentrations *i.e.* 62.5, 125, 250, and 500 μg ml^{-1}, inhibited both qualitative (Fig. 6A) and quantitative (Fig. 6B) production of violacein by *C. violaceum* in a dose-dependent manner controlling the quorum sensing which is a primary factor for the development of biofilm and bacterial virulence.[61] Zone of violacein depigmentation on agar media was found statistically significant ($P \leq 0.05$) at all concentrations, whereas, the significance of inhibition of violacein

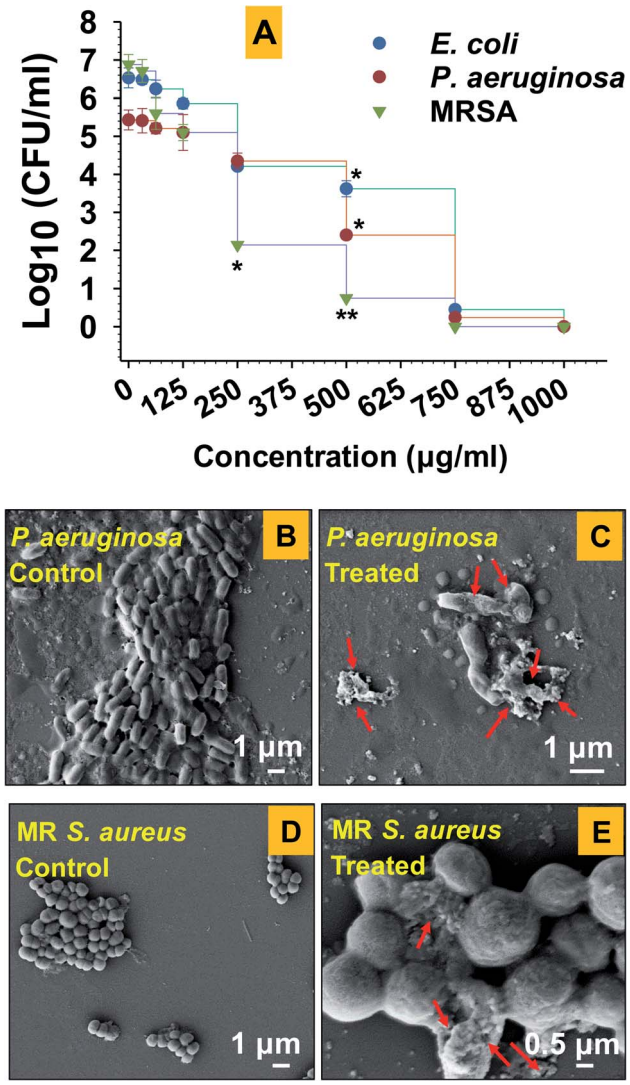

Fig. 5 Reduction in log_{10} CFU ml^{-1} of pathogenic bacterial cells (panel A), SEM micrographs of untreated *P. aeruginosa* (panel B), treated with 500 μg ml^{-1} GT-Fe_2O_3 nanoparticles (panel C), untreated MR *S. aureus* (panel D), and treated with 500 μg ml^{-1} GT-Fe_2O_3 nanoparticles (panel E). Red arrows in panels C and E indicate destruction of bacterial morphology by nanoparticles over untreated control. '*' and '**' show statistical significance at $P \leq 0.05$ and $P \leq 0.01$, respectively over untreated control.

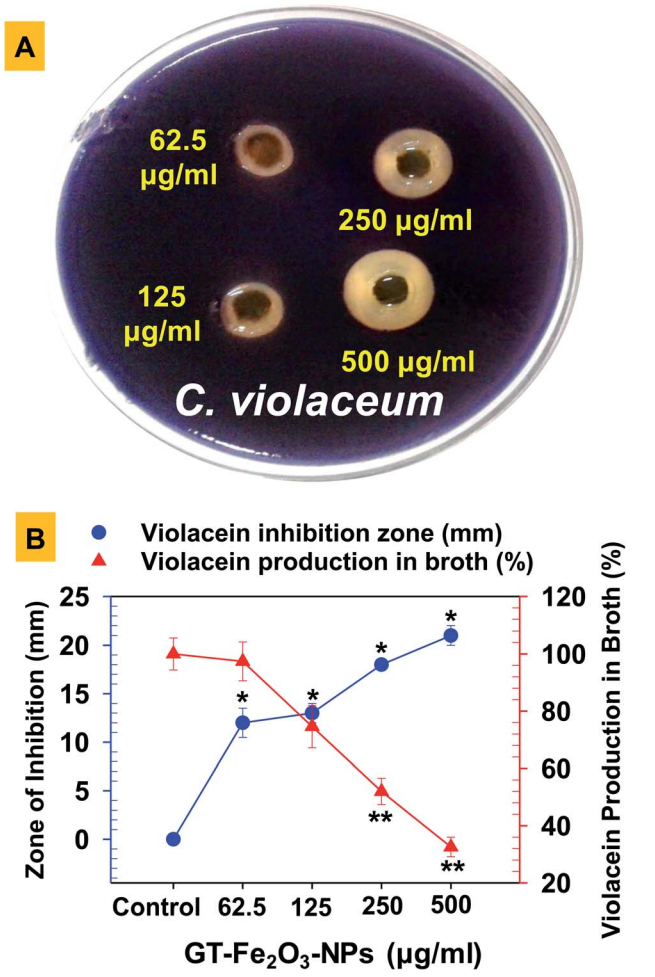

Fig. 6 Qualitative (panel A) and quantitative inhibition (panel B) of violacein production by *C. violaceum* under GT-Fe_2O_3 nanoparticle (NP) stress. Error bars represent standard deviation from at least three replicates. '*' and '**' show statistical significance at $P \leq 0.05$ and $P \leq 0.01$, respectively over untreated control.

production in the broth was $P \leq 0.05$ at 125 μg ml^{-1} and $P \leq 0.01$ at 250 μg ml^{-1} and 500 μg ml^{-1} GT-Fe_2O_3 nanoparticles. Similar results have been discussed with other nanoparticles such as AgCl–TiO_2 nanoparticles at 100–500 μg ml^{-1}[59] and ZnO and TiO_2 nanoparticles at 10–500 μg ml^{-1}.[62] Two different QS system found in *P. aeruginosa* governed by cell-to-cell communication such as swarming motility and pyocyanin production were inhibited by ZnO-NPs significantly at 12.5–100 μg ml^{-1} and 50–100 μg ml^{-1}, respectively.[63]

Growing cases of MDR in bacteria associated with biofilm formation by ESβL *E. coli* and *P. aeruginosa* and methicillin-resistant (MR) *S. aureus* is a global clinical challenge. Therefore, the assessment of biofilm formation by these strains under GT-Fe_2O_3 nanoparticles stress was done on the glass surface (Fig. 7A) and in polystyrene microtiter plate (Fig. 7B) at MIC and two sub-MIC concentrations. The data revealed that biofilm formation in both experimental settings decreased in a dose-dependent manner. Thus, reduction in bacterial activity was also supported by the destruction of biofilms formed by *E. coli*, *P. aeruginosa*, and MRSA at MIC ($P \leq 0.05$), $\frac{1}{2}$ MIC ($P \leq 0.05$) and $\frac{1}{4}$ MIC as compared to untreated control (Fig. 7A). The inhibition was found statistically significant ($P \leq 0.05$) at $\frac{1}{2}$ MIC and MIC of GT-Fe_2O_3 nanoparticles (Fig. 7B). Inhibition of bacterial strains was in the following order: *P. aeruginosa* > MRSA > *E. coli*. These results reveal the antibiofilm potency of GT-Fe_2O_3 nanoparticles and corroborate with the earlier findings of biofilm inhibition by some metal oxide nanoparticles. Few examples are *E. coli*, *P. aeruginosa*, and *S. aureus* biofilm inhibition by ZnO nanoparticles,[40] CuO nanoparticles,[64] and NiO nanoparticles.[38] In another study, significantly high reduction in biofilm formation by *P. aeruginosa* (63.43%) and *Staphylococcus epidermidis* (62.88%) at 100 μg ml^{-1} ZnO-NPs was reported.[63] This could be well corelated with the inhibition of QS regulation system as shown by arrest of swarming motility and pyocyanin production by *P. aeruginosa*. Mechanistically, the antibacterial behavior of nanoparticles lies in their smaller size which allows them to wrap the microbial cell surface and lowers the O_2 supply thus inhibiting cellular respiration.[53] Induction of oxidative stress is yet another cause of the microbial killing. Reactive oxygen species ($O_2^{\bullet -}$, $-OH^{\bullet}$, H_2O_2, and $^1O_2$) generation by Fenton reaction as a result of iron oxide nanoparticles stress can induce DNA and protein damage in microbial cells.[65,66] Moreover, due to its reducing capacity, iron nanoparticles may decompose the functional moieties of membrane lipopolysaccharides and proteins.

3.4 Antifungal and anticancer activity of GT-Fe_2O_3 nanoparticles

To assess the broad-spectrum inhibitory activity of GT-Fe_2O_3 nanoparticles, the nanoparticles were further tested against two other organisms including a fungus (*F. oxysporum*) and a human cancer cell line (MCF-7 cells). The antifungal potential of nanoparticles (125–1000 μg ml^{-1}) against *F. oxysporum* recorded after six days of exposure showed a substantial reduction in radial mycelial growth over untreated control (Fig. 8A). Quantification of mycelial growth at 250 μg ml^{-1} was significant at $P \leq 0.05$ whereas, at 500 and 1000 μg ml^{-1}, P value was found as ≤0.01. The fungal inhibition was dose-dependent due to the fact that among other factors (composition, size, and shape), nanoparticle activity depends on exposure concentration. Nanoparticles may completely retard the growth of fungi by targeting and destructing the cell membrane structure and

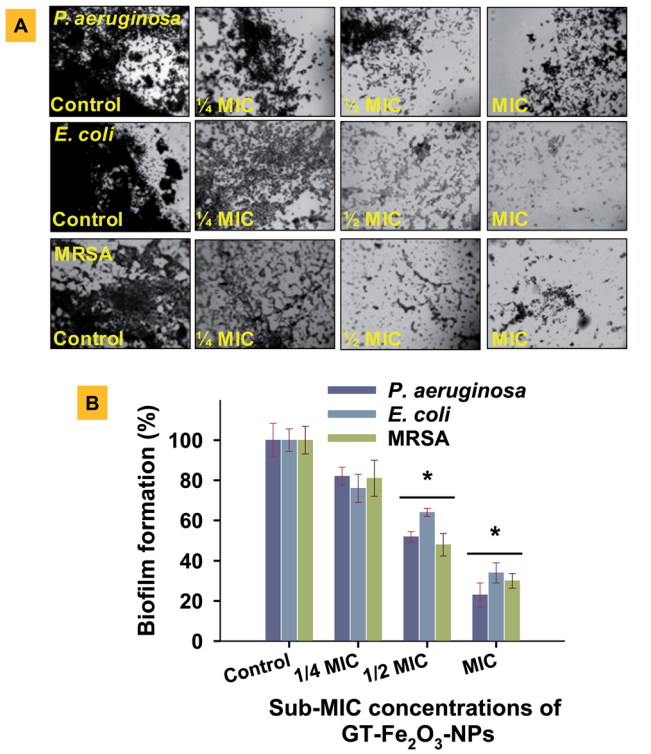

Fig. 7 Inhibition of biofilm formation by GT-Fe_2O_3 nanoparticles (NPs) on glass cover slip (A) and percent reduction in biofilm formation (B). Error bars represent standard deviation from at least three replicates while '*' shows statistical significance at $P \leq 0.05$.

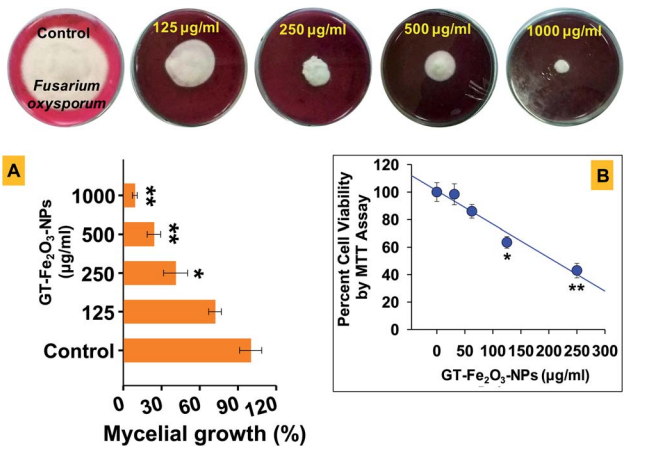

Fig. 8 Antifungal activity of GT-Fe_2O_3 nanoparticles (NPs) against *F. oxysporum* (A) and cytotoxic activity against MCF-7 cells (B). Error bars represent standard deviation from at least three replicates while '*' and '**' show statistical significance at $P \leq 0.05$ and $P \leq 0.01$, respectively over untreated control.

Table 3 Comparative analysis of results of this study with available literature

S. no.	Method of synthesis	Size (nm)	Morphology	Crystal phase by XRD	Effective concentration (mg ml^{-1}) against			Inhibition of quorum sensing (QS)	Synergism with antibiotics	Reference
					MDR bacteria	Fungi	Cancer cells			
1	Gallo-tannin mediated, co-precipitation of $FeSO_4$ and $FeCl_3$	12.85	Predominantly spherical	Rhombohedrally centered hexagonal structure	0.25–0.75	0.125–1.0	0.125	Inhibited QS at 0.25–0.5 mg ml^{-1}	Enhanced bacterial killing of antibiotics	**Current study**
2	Tannic acid in alkali medium, co-precipitation of $FeSO_4$ and $FeCl_3$	10–30	Circular	Mixed hexagonal phase of Fe_2O_3 and Fe_3O_4 NPs	Not assessed	0.2–0.5	Not assessed	Not assessed	Not assessed	65
3	Co-precipitation of $FeCl_2$ and $FeCl_3$ followed by addition of tannic acid	8–30	Polydisperse with shapes spherical, hexagonal, pentagonal, rectangular, and triangular	Cubic inverse spinel structure	Not assessed	Not assessed	Not assessed	Not assessed	Not assessed	79
4	Tannic acid mediated synthesis in alkaline medium using $Fe(NO_3)_3 \cdot 9H_2O$	30–50	Spherical	Mixed crystalline phase of magnetite and hematite	Not assessed	Not assessed	Not assessed	Not assessed	Not assessed	18
5	Synthesis using *Gardenia resinifera* extract and $FeCl_3 \cdot 6H_2O$	3–8	Spherical	Pure α-Fe_2O_3 phase	Not assessed	Not assessed	Biocompatible with human mesenchymal cells even at 1 mg ml^{-1}	Not assessed	Not assessed	80
6	Green synthesis using *Rhus punjabensis* extract and $FeCl_3$	~48	Spherical	α-Fe_2O_3 phase	Very low antibacterial activity	Not assessed	Significant cytotoxicity against DU-145 and HL60 cell lines with IC_{50} of 12.79 and 11.96 mg ml^{-1}, respectively	Not assessed	Not assessed	81
7	Green synthesis using *Sida cordifolia* extract and $Fe(NO_3)_3$	10–22	Spherical nano clusters	Rhombohedral hematite phase of α-Fe_2O_3 NPs	Zone of bacterial growth of inhibition at 50 μg ml^{-1} on agar wells	Not assessed	Not assessed	Not assessed	Not assessed	27
8	Green synthesis using *Plectranthus amboinicus* extract and $FeCl_3$	80–100	Small spherical shapes	Rhombohedral α-Fe_2O_3 NPs	Low antibacterial activity by agar well diffusion method	Low antifungal activity by agar well diffusion method	Not assessed	Not assessed	Not assessed	82

impeding the cell division.[67] For example, green synthesized ZnO-NPs have been suggested to interact and damage the fungal cell membrane inducing cellular bulging, compromising membrane integrity and reducing its smoothness in a concentration dependent manner.[68] Further, the GT-Fe_2O_3 nanoparticles can be expected to damage fungal cellular structure by inducing DNA loss, altered expression of ribosome related proteins, and indirectly inhibiting ATP production by obstructing essential enzyme production.[69] In a similar study, iron oxide nanoparticles have been reported to hinder the growth of *F. solani* and *A. niger*.[70]

The GT-Fe_2O_3 nanoparticles at 62.5–250 μg ml^{-1} also induced dose-related cytotoxicity in MCF-7 cancer cells co-cultivated with GT-Fe_2O_3 nanoparticles (Fig. 8B) as observed by MTT assay. This assay quantifies the activity of cellular oxidoreductase enzymes (NADPH mediated) which reduce the MTT to insoluble formazan and thus provide information about the metabolic activity of viable cells.[71] The difference between effective inhibitory concentration between fungal cells (250–1000 μg ml^{-1}) and MCF-7 cells (125–250 μg ml^{-1}) could be due to the absence of cell wall in MCF-7 cells and the difference in lipid composition in cell membrane.[72,73] Similarly, Fe_2O_3 nanoparticles synthesized by other methods have shown antifungal and anticancer activities.[74] Moreover, the spherical iron oxide nanoparticles have also exhibited concentration-dependent growth arrest in murine macrophage cell line.[75] In another study, MCF-7 cells actively took up the iron oxide nanoparticles which then induced intracellular oxidative stress and caused cell membrane injury.[30] Fe_2O_3-NPs share common anticancer cytotoxicity properties with other metal-oxide nanoparticles such as Ag doped ZnO NPs caused cancer cell shrinkage, rounding, and loss of attachment with adjacent cells,[76] Similarly, CeO_2-NPs against MCF-7 cells,[77] Co_3O_4-NPs against human glioblastoma U-87 MG cells[78] which were attributed to the significant intracellular accumulation of nanoparticles. A comparative analysis of our results with the literature is summarized in Table 3.

4 Conclusion

The gallo-tannin capped Fe_2O_3 nanoparticles were successfully synthesized by co-precipitating two iron salts ($FeCl_3$ and $FeSO_4$) while simultaneously capping them by gallo-tannin at low temperature. The physicochemical characterization of GT-Fe_2O_3 nanoparticles by state-of-the-art techniques including AFM, SEM, TEM, EDX, FT-IR, and UV-Vis revealed pleomorphism in shape with some spherical nanoparticles. On the application aspect, GT-Fe_2O_3 nanoparticles (12.85 nm) proved to be useful as an efficient antibacterial agent limiting the growth and biofilm formation of multi-drug resistant clinical bacteria causing chronic infections. The biofilm was disrupted by stopping the quorum sensing ability of bacteria. GT-Fe_2O_3 nanoparticles also restored the antibacterial potential of antibiotics. Moreover, these nanoparticles showed promising antifungal and anticancer activities against the world's fourth major cancer-causing cells (MCF-7). This study for the first time has focused on the detailed biomedical applications of gallo-tannin capped Fe_2O_3 nanoparticles. Therefore, GT-Fe_2O_3 nanoparticles are envisaged as a promising alternative for biomedical applications.

Conflicts of interest

The authors declare that there are no conflicts of financial or personal interest.

Acknowledgements

This work was supported by the Yeungnam University Research Grant. The authors extend their appreciation to the Deanship of Scientific Research, King Saud University for funding this work through research group No (RG-1440-056).

References

1 A. Azam, A. S. Ahmed, M. Oves, M. S. Khan, S. S. Habib and A. Memic, *Int. J. Nanomed.*, 2012, **7**, 6003.
2 S. A. Ansari, M. Oves, R. Satar, A. Khan, S. I. Ahmad, M. A. Jafri, S. K. Zaidi and M. H. Alqahtani, *Pol. J. Chem. Technol.*, 2017, **19**(4), 110–115.
3 A. Ali, H. Zafar, M. Zia, I. ul Haq, A. R. Phull, J. S. Ali and A. Hussain, *Nanotechnol., Sci. Appl.*, 2016, **9**, 49–67.
4 N. M. Dissanayake, K. M. Current and S. O. Obare, *Int. J. Mol. Sci.*, 2015, **16**, 23482–23516.
5 M. Hasan, G. Mustafa, J. Iqbal, M. Ashfaq and N. Mahmood, *J. Toxicol. Res.*, 2018, **7**(1), 84–92.
6 A. M. G. C. Dias, A. Hussain, A. S. Marcos and A. C. A. Roque, *Biotechnol. Adv.*, 2011, **29**(1), 142–155.
7 B. Chertok, B. A. Moffat, A. E. David, F. Yu, C. Bergemann, B. D. Ross and V. C. Yang, *Biomaterials*, 2008, **29**(4), 487–496.
8 O. C. Wilson, E. Blair, S. Kennedy, G. Rivera and P. Mehl, *Mater. Sci. Eng. C*, 2008, **28**(3), 438–442.
9 L. Kvítek, A. Panáček, J. Soukupová, M. Kolář, R. Večeřová, R. Prucek, M. Holecová and R. Zbořil, *J. Phys. Chem. C*, 2009, **113**(11), 4296–4300.
10 M. Krispin, A. Ullrich and S. Horn, *J. Nanoparticle Res.*, 2012, **14**(2), 1.
11 E. A. Campos, D. V. B. S. Pinto, J. I. S. de Oliveira, E. da C. Mattos and R. de C. L. Dutra, *J. Aerosp. Technol. Manage.*, 2015, **7**(3), 267–276.
12 R. Periakaruppan, X. Chen, K. Thangaraj, A. Jeyaraj, H. H. Nguyen, Y. Yu, S. Hu, L. Lu and X. Li, *J. Cleaner Prod.*, 2021, **278**, 123962.
13 D. Mukherjee, S. Ghosh, S. Majumdar and K. Annapurna, *J. Environ. Chem. Eng.*, 2016, **4**(1), 639–650.
14 D. Patiño-Ruiz, L. Sánchez-Botero, L. Tejeda-Benitez, J. Hinestroza and A. Herrera, *Environ. Nanotechnol. Monit. Manag.*, 2020, **14**, 100377.
15 J. A. A. Abdullah, L. Salah Eddine, B. Abderrhmane, M. Alonso-González, A. Guerrero and A. Romero, *Sustainable Chem. Pharm.*, 2020, **17**, 100280.
16 M. Aghazadeh, I. Karimzadeh and M. R. Ganjali, *Mater. Lett.*, 2018, **228**, 137–140.

17 E. Amanzadeh, A. Esmaeili, R. E. N. Abadi, N. Kazemipour, Z. Pahlevanneshan and S. Beheshti, *Sci. Rep.*, 2019, **9**, 6876.
18 H. S. Devi and T. D. Singh, *Perspect Sci.*, 2016, **8**, 287–289.
19 J. Tanwar, S. Das, Z. Fatima and S. Hameed, *Interdiscip. Perspect. Infect. Dis.*, 2014, **541340**, 1–7.
20 S. Ahmed, J. Ning, D. Peng, T. Chen, I. Ahmad, A. Ali, Z. Lei, M. Abu bakr Shabbir, G. Cheng and Z. Yuan, *Food Agric. Immunol.*, 2020, **31**(1), 268–290.
21 Y. Song, W. Zhang, S. He, L. Shang, R. Ma, L. Jia and H. Wang, *ACS Appl. Mater. Interfaces*, 2019, **11**(37), 33676–33683.
22 Y. Li, W. Zhang, J. Niu and Y. Chen, *ACS Nano*, 2012, **6**(6), 5164–5173.
23 S. Kheiri, X. Liu and M. Thompson, *Colloids Surf., B*, 2019, **184**, 110550.
24 M. Alavi and M. Rai, *Expert Rev. Anti-Infect. Ther.*, 2019, **17**(6), 419–428.
25 N. Tran, A. Mir, D. Mallik, A. Sinha, S. Nayar and T. J. Webster, *Int. J. Nanomed.*, 2010, **5**, 277.
26 M. H. Moshafi, M. Ranjbar and G. Ilbeigi, *Int. J. Nanomed.*, 2019, **14**, 3273.
27 P. N. V. K. Pallela, S. Ummey, L. K. Ruddaraju, S. Gadi, C. S. L. Cherukuri, S. Barla and S. V. N. Pammi, *Heliyon*, 2019, **5**(11), e02765.
28 A. Saranya, A. Thamer, K. Ramar, A. Priyadharsan, V. Raj, K. Murugan, A. Murad and P. Maheshwaran, *J. Photochem. Photobiol., B*, 2020, **207**, 111885.
29 F. Xu, F. Wang, T. Yang, Y. Sheng, T. Zhong and Y. Chen, *Cancer Cell Int.*, 2014, **14**, 142.
30 Y. Zhang, Y. Hai, Y. Miao, X. Qi, W. Xue, Y. Luo, H. Fan and T. Yue, *Food Chem.*, 2021, **341**, 128263.
31 M. van der Zande, A. K. Undas, E. Kramer, M. P. Monopoli, R. J. Peters, D. Garry, E. C. Antunes Fernandes, P. J. Hendriksen, H. J. P. Marvin, A. A. Peijnenburg and H. Bouwmeester, *Nanotoxicology*, 2016, **10**(10), 1431–1441.
32 K. Ali, Q. Saquib, B. Ahmed, M. A. Siddiqui, J. Ahmad, M. Al-Shaeri, A. A. Al-Khedhairy and J. Musarrat, *Process Biochem.*, 2020, **91**, 387–397.
33 H. E. A. Mohamed, S. Afridi, A. T. Khalil, M. Ali, T. Zohra, M. Salman, A. Ikram, Z. K. Shinwari and M. Maaza, *Mater. Sci. Eng. C*, 2020, **112**, 110890.
34 W. Muhammad, M. A. Khan, M. Nazir, A. Siddiquah, S. Mushtaq, S. S. Hashmi and B. H. Abbasi, *Mater. Sci. Eng. C*, 2019, **103**, 109740.
35 B. Ahmed, F. Ameen, A. Rizvi, K. Ali, H. Sonbol, A. Zaidi, M. S. Khan and J. Musarrat, *ACS Omega*, 2020, **5**, 7861–7876.
36 W. Kirby, A. Bauer, J. Sherris and M. Turk, *Am. J. Clin. Pathol.*, 2000, **42**(3–4), 208–272.
37 CLSI, *Performance Standards for Antimicrobial Susceptibility Testing CLSI supplement M100S*, 2016, p. 256.
38 S. Saleem, B. Ahmed, M. S. Khan, M. Al-Shaeri and J. Musarrat, *Microb. Pathog.*, 2017, **111**, 375–387.
39 N. Valarmathi, F. Ameen, A. Almansob, P. Kumar, S. Arunprakash and M. Govarthanan, *Mater. Lett.*, 2020, **263**, 127244.
40 B. Ahmed, B. Solanki, A. Zaidi, M. S. Khan and J. Musarrat, *J. Toxicol. Res.*, 2019, **8**, 246–261.
41 S. Saleem, B. Ahmed, M. S. Khan, M. Al-Shaeri and J. Musarrat, *Microb. Pathog.*, 2017, **111**, 375–387.
42 M. Dolci, J. F. Bryche, J. Moreau, C. Leuvrey, S. Begin-Colin, G. Barbillon and B. P. Pichon, *Appl. Surf. Sci.*, 2020, **527**, 146773.
43 X. S. Wang, X. Liu, L. Wen, Y. Zhou, Y. Jiang and Z. Li, *Sep. Sci. Technol.*, 2008, **43**(14), 3712–3731.
44 S. Kundu and U. Nithiyanantham, *RSC Adv.*, 2013, **3**(47), 25278–25290.
45 K. K. Hoskote Anand and B. K. Mandal, *Spectrochim. Acta, Part A*, 2015, **135**, 639–645.
46 R. Zboril, L. MacHala, M. Mashlan and M. Hermanek, *AIP Conf. Proc.*, 2005, **765**, 757.
47 L. Pauling and S. B. Hendricks, *J. Am. Chem. Soc.*, 1925, **47**(3), 781–790.
48 W. Aidi Wannes, B. Mhamdi, J. Sriti, M. Ben Jemia, O. Ouchikh, G. Hamdaoui, M. E. Kchouk and B. Marzouk, *Food Chem. Toxicol.*, 2009, **112**(3), 621–626.
49 S. A. O. Santos, J. J. Villaverde, C. S. R. Freire, R. M. M. Domingues, C. P. Neto and A. J. D. Silvestre, *Ind. Crops Prod.*, 2012, **39**, 120–127.
50 K. Mohan Kumar, B. K. Mandal, K. Siva Kumar, P. Sreedhara Reddy and B. Sreedhar, *Spectrochim. Acta, Part A*, 2013, **102**, 128–133.
51 A. H. Wani, M. Amin, M. Shahnaz and M. A. Shah, *Int. J. Manuf. Mater. Mech. Eng.*, 2012, **2**(4), 59–70.
52 D. Rawat and D. Nair, *J. Global Infect. Dis.*, 2010, **2**(3), 263.
53 S. Abdeen, R. S. Rimal Isaac, S. Geo, S. Sornalekshmi, A. Rose and P. K. Praseetha, *Nano Biomed. Eng.*, 2013, **5**, 1.
54 S. J. Kim, J. Chang and M. Singh, *Biochim. Biophys. Acta Biomembr.*, 2015, **1848**(1), 350–362.
55 T. Naseem and T. Durrani, *J. Environ. Chem. Ecotoxicol.*, 2021, **3**, 59–75.
56 S. Ravikumar, R. Gokulakrishnan and P. Boomi, *Asian Pac. J. Trop. Dis.*, 2012, **2**(2), 85–89.
57 G. Basak, D. Das and N. Das, *J. Microbiol. Biotechnol.*, 2014, **24**(1), 87–96.
58 W. R. Li, Y. K. Ma, X. B. Xie, Q. S. Shi, X. Wen, T. L. Sun and H. Peng, *Front. Microbiol.*, 2019, **9**, 3222.
59 K. Naik and M. Kowshik, *J. Appl. Microbiol.*, 2014, **117**(4), 972–983.
60 M. Venkatramanan, P. Sankar Ganesh, R. Senthil, J. Akshay, A. Veera Ravi, K. Langeswaran, J. Vadivelu, S. Nagarajan, K. Rajendran and E. M. Shankar, *ACS Omega*, 2020, **5**(40), 25605–25616.
61 S. Pattnaik, T. Ahmed, S. K. Ranganathan, D. R. Ampasala, V. V. Sarma and S. Busi, *Biofouling*, 2018, **34**, 410–425.
62 B. Gómez-Gómez, L. Arregui, S. Serrano, A. Santos, T. Pérez-Corona and Y. Madrid, *Sci. Total Environ.*, 2019, **696**, 133869.
63 M. Alavi, N. Karimi and I. Salimikia, *J. Ind. Eng. Chem.*, 2019, **72**, 457–473.
64 K. Ali, B. Ahmed, S. M. Ansari, Q. Saquib, A. A. Al-Khedhairy, S. Dwivedi, M. Alshaeri, M. S. Khan and J. Musarrat, *Mater. Sci. Eng. C*, 2019, **100**, 747–758.
65 S. Parveen, A. H. Wani, M. A. Shah, H. S. Devi, M. Y. Bhat and J. A. Koka, *Microb. Pathog.*, 2018, **115**, 287–292.

66 Y. M. Mohamed, A. M. Azzam, B. H. Amin and N. A. Safwat, *African J. Biotechnol.*, 2015, **14**, 14.
67 K. J. Kim, W. S. Sung, B. K. Suh, S. K. Moon, J. S. Choi, J. G. Kim and D. G. Lee, *BioMetals*, 2009, **22**(2), 235–242.
68 A. Miri, N. Mahdinejad, O. Ebrahimy, M. Khatami and M. Sarani, *Mater. Sci. Eng. C*, 2019, **104**, 109981.
69 S. W. Kim, J. H. Jung, K. Lamsal, Y. S. Kim, J. S. Min and Y. S. Lee, *Mycobiology*, 2009, **93**(10), 1037–1043.
70 P. Nehra, R. P. Chauhan, N. Garg and K. Verma, *Br. J. Biomed. Sci.*, 2018, **75**(1), 13–18.
71 S. Ramasamy, I. V. M. V. Enoch and S. Rex Jeya Rajkumar, *Mater. Lett.*, 2020, **261**, 127114.
72 W. Szlasa, I. Zendran, A. Zalesińska, M. Tarek and J. Kulbacka, *J. Bioenerg. Biomembr.*, 2020, **52**, 321–342.
73 M. Del Poeta, S. F. Chen, D. Von Hoff, C. C. Dykstra, M. C. Wani, G. Manikumar, J. Heitman, M. E. Wall and J. R. Perfect, *Antimicrob. Agents Chemother.*, 1999, **43**(12), 2862–2868.
74 V. Ramalingam, M. Harshavardhan, S. Dinesh Kumar and S. Malathi devi, *J. Alloys Compd.*, 2020, **834**, 155118.
75 S. Naqvi, M. Samim, M. Z. Abdin, F. J. Ahmed, A. N. Maitra, C. K. Prashant and A. K. Dinda, *Int. J. Nanomed.*, 2010, **5**, 983.
76 R. Rajendran and A. Mani, *J. Saudi Chem. Soc.*, 2020, **24**(12), 1010–1024.
77 M. Sridharan, P. Kamaraj, Vennilaraj, J. Arockiaselvi, T. Pushpamalini, P. A. Vivekanand and S. Hari Kumar, *Mater. Today: Proc.*, 2021, **36**(4), 914–919.
78 X. Huang, H. Cai, H. Zhou, T. Li, H. Jin, C. E. Evans, J. Cai and J. Pi, *Acta Biomater.*, 2021, **121**, 605–620.
79 A. F. M. Santos, L. J. A. Macedo, M. H. Chaves, M. Espinoza-Castañeda, A. Merkoçi, F. D. C. A. Limac and W. Cantanhêde, *J. Braz. Chem. Soc.*, 2016, **27**(4), 727–734.
80 V. C. Karade, S. B. Parit, V. V. Dawkar, R. S. Devan, R. J. Choudhary, V. V. Kedge, N. V. Pawar, J. H. Kim and A. D. Chougale, *Heliyon*, 2019, **5**(7), e02044.
81 S. Naz, M. Islam, S. Tabassum, N. F. Fernandes, E. J. Carcache de Blanco and M. Zia, *J. Mol. Struct.*, 2019, **1185**, 1–7.
82 R. Ramesh, V. Yamini, D. Rajkumar, S. John Sundaram, D. Lakshmi and F. L. A. Khan, *Mater. Today: Proc.*, 2021, **36**, 453–458.